thermo

MDPI

Article

Coupled Irreversibilities and Asymmetric Dissipation in Liquid-State Thermocells

Xiongxiong Wu *, Zhimin Yang and Yanning Yang

School of Physics and Electronic Information, Yan'an University, Yan'an 716000, China; yzm@yau.edu.cn (Z.Y.); yadxyyn@163.com (Y.Y.)
* Correspondence: wuxx1992yygx@126.com

Abstract

Liquid-state thermocells (LTCs) are emerging electrochemical heat engines for harvesting low-grade thermal energy across small temperature differences. Their practical performance is jointly limited by internal dissipation associated with ionic and electrochemical transport, as well as by external irreversibility arising from finite thermal coupling to the heat source and sink. In this work, a finite-rate thermodynamic framework is developed for LTCs subject to coupled internal and external irreversibilities. The model combines effective thermoelectrochemical transport, a phenomenological asymmetric Joule-heat partition parameter motivated by electrode and interfacial heat effects, and non-ideal thermal contacts, thereby enabling analytical optimization of power output in four representative configurations. Closed-form expressions are derived for the maximum power and the efficiency at maximum power (EMP), together with the admissible operating domain and an equivalent-circuit interpretation. The results show that the thermal impedance ratio governs a transition between externally limited and internally limited regimes. In the externally dominated limit, all configurations recover the Curzon–Ahlborn efficiency, whereas in the internally dominated limit, the asymptotic EMP depends on the side receiving irreversible heat release. When both dominant irreversibilities are located on the hot side, the highest EMP is achieved, while the opposite configuration yields the lowest EMP. These findings provide a thermodynamic benchmark for the LTC architecture and clarify how thermal contact asymmetry and internal heat release pathways should be coordinated to enhance performance in low-grade heat recovery.

Keywords: liquid-state thermocell; finite-time thermodynamics; efficiency at maximum power; Joule heat partition; thermal impedance matching

Check for updates

Academic Editor: Steve Lustig

Received: 20 April 2026
Revised: 24 May 2026
Accepted: 28 May 2026
Published: 1 June 2026

Copyright: © 2026 by the authors. Licensee MDPI, Basel, Switzerland. This article is an open access article distributed under the terms and conditions of the Creative Commons Attribution (CC BY) license.

1. Introduction

The conversion of low-grade heat into electricity plays an increasingly important role in industrial energy efficiency and sustainable energy systems [1–3]. A large portion of consumed energy is ultimately dissipated as waste heat at relatively low temperatures, where conventional recovery technologies are often inefficient or economically unattractive [4]. This motivated the development of heat-to-electricity devices capable of operating efficiently across small temperature differences [5–7].

Liquid-state thermocells (LTCs), also known as thermogalvanic cells, have recently attracted considerable attention as promising candidates for low-grade heat recovery [8–10]. Unlike solid-state thermoelectric devices, LTCs convert thermal energy into electricity through temperature-dependent redox reactions occurring in an electrolyte

between two electrodes [11–13]. In the $K_3Fe(CN)_6/K_4Fe(CN)_6$ electrolyte system, the $Fe(CN)_6^{3-}/Fe(CN)_6^{4-}$ couple undergoes oxidation at the hot electrode and reduction at the cold electrode [14–16], establishing a potential difference that generates electrical current through an external circuit, as shown in Figure 1. Owing to their intrinsic characteristics, LTCs offer several advantages, including low material cost, chemical tunability, ease of fabrication, and relatively good performance under small temperature differences [17]. These features make them particularly attractive for distributed energy harvesting and low-grade heat recovery applications [18–20]. Despite these advantages, the performance of practical LTCs remains far below the thermodynamic limit. This discrepancy arises from the presence of multiple irreversible processes that act simultaneously within the system [21]. Internally, energy dissipation originates from ionic transport resistance, interfacial charge transfer processes, and Joule heating. Externally, finite thermal conductance between the cell and the heat reservoirs reduces the effective temperature difference across the electrochemically active region [22]. In addition, parasitic heat leakage through the electrolyte and structural components further degrades the energy conversion efficiency [23]. Since these internal and external irreversibilities are inherently coupled, a comprehensive theoretical framework is required to understand their combined impact on LTC performance.

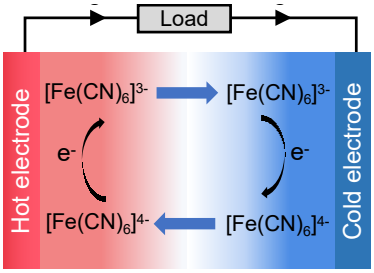


Figure 1. Operating principle of a liquid-state thermocell. A temperature difference between the hot and cold electrodes drives temperature-dependent redox reactions, generating an electromotive force and electrical current through an external load.

Finite-time thermodynamics provides a powerful tool for analyzing the performance of heat engines operating under irreversible conditions [24–26]. Two classical limiting results are well established. When irreversibility is dominated by finite-rate heat transfer between the system and the reservoirs, the efficiency at maximum power is given by the Curzon−Ahlborn efficiency [27]. In contrast, when internal dissipation is the dominant irreversibility, the corresponding efficiency follows the Schmiedl−Seifert relation [28,29]. These two limits define the upper and lower bounds for a wide class of irreversible heat engines. However, real LTC systems typically operate in an intermediate regime in which both internal and external irreversibilities coexist and interact. Their performance cannot be adequately described by either limiting case alone. For solid-state thermoelectric generators, several studies have investigated the combined effects of internal and external irreversibilities within finite-time thermodynamic frameworks [30–33]. In particular, Kaur and Johal developed an exactly solvable model that accounts for asymmetric placement of external thermal resistance and Joule-heat dissipation, leading to analytical expressions for maximum power and efficiency at maximum power in different configurations [34]. Their work provides a valuable theoretical foundation for understanding how the spatial distribution of irreversibilities influences heat engine performance. However, LTCs differ fundamentally from solid-state thermoelectric systems in both physical mechanisms and transport processes [17,35]. The effective Seebeck coefficient in LTCs originates from thermoelectrochemical effects rather than carrier diffusion in solids, and the internal resistance includes contributions from ionic conduction and interfacial kinetics [36]. More importantly, the spatial distribution of irreversible heat release in LTCs can be strongly

influenced by electrochemical reactions, electrolyte properties, and thermal coupling conditions [37]. As a result, the direct application of thermoelectric generator models to LTC systems may obscure key physical insights specific to liquid-state electrochemical energy conversion. The possibility of spatially asymmetric heat release is also consistent with classical thermocell theory. Holtan, Mazur, and de Groot showed that heat and entropy changes in thermocells are closely related to electrochemical potential differences and electrode processes [36], while Ratkje et al. further clarified that heat and internal energy changes at electrodes and junctions may differ from the bulk Joule contribution [37]. These studies indicate that heat release in thermocells is not necessarily spatially symmetric but can depend on electrode reactions, interfacial energy conversion, and junction effects. This provides a physical basis for introducing an effective heat partition parameter in a reduced thermodynamic description.

To address these issues, the present work develops a thermodynamic framework specifically tailored to liquid-state thermocells under coupled internal and external irreversibilities. Building on the analytical structure of exactly solvable models, we reinterpret the governing parameters in terms of LTC physics and introduce an asymmetric Joule-heat partition parameter to describe directional irreversible heat release. This approach enables a systematic investigation of how the placement of thermal resistance and irreversible heat affects power generation and efficiency. Four representative configurations are analyzed, corresponding to different combinations of thermal contact asymmetry and Joule-heat distribution. For each configuration, analytical expressions for the maximum power, efficiency at maximum power, and operating constraints are derived. In addition, the role of the thermal impedance ratio in governing the transition between externally limited and internally limited regimes is clarified. The main contributions of this work are summarized as follows: (1) the development of a unified thermodynamic model for LTCs incorporating coupled internal and external irreversibilities; (2) the introduction of an asymmetric Joule-heat partition parameter with clear physical interpretation in electrochemical systems; (3) the derivation of exact analytical expressions for maximum power and efficiency at maximum power in four benchmark configurations; and (4) the identification of performance limits and design guidelines for optimizing the LTC architecture. These results provide a theoretical basis for understanding the interplay between different irreversible processes in LTCs and offer guidance for the design and optimization of liquid-state electrochemical heat engines.

2. Methods

2.1. The LTC System and Effective Transport Description

We considered a one-dimensional LTC of a length L and cross-sectional area A thermally coupled to a hot reservoir at a temperature T_h and a cold reservoir at a temperature T_c, with $T_h > T_c$, as shown in Figure 2. The local temperatures of the active thermocell region at the hot and cold sides are denoted by T_{hs} and T_{cs}, respectively. The cell was characterized by an effective thermoelectrochemical Seebeck coefficient S_e, an intrinsic electrical resistance R, and an effective internal thermal conductance K. Here, S_e should be understood as the redox-entropy-driven thermopower of the LTC rather than the carrier-based Seebeck coefficient of a solid-state thermoelectric material. Likewise, R denotes an effective intrinsic electrical resistance that may include the ionic resistance of the electrolyte, separator resistance, interfacial charge transfer resistance, and other ohmic losses under steady operating conditions. The thermal coupling to the external reservoirs is represented by the hot-side and cold-side thermal conductances K_h and K_c, respectively. Throughout this work, K, K_h, and K_c denote thermal conductances with units of W K^{-1}, whereas $\kappa(x)$ denotes a local thermal conductivity with units of W m^{-1} K^{-1}. In the main text, J denotes

the total electrical current flowing through the external circuit, whereas j denotes the local current density used only in the local transport derivation in Appendix A. These two quantities are related by $J = jA$. Accordingly, $\dot{Q}_h$, $\dot{Q}_c$, and P in the main text represent terminal heat currents and electrical power, rather than local heat flux densities.

Within the Onsager−Callen−Domenicali framework [38–41], the heat currents at the hot and cold ends of the active region may be written as follows:

$$\dot{Q}_h = JS_eT_{hs} + K(T_{hs} - T_{cs}) - \frac{1}{2}J^2R, \tag{1}$$

$$\dot{Q}_c = JS_eT_{cs} + K(T_{hs} - T_{cs}) + \frac{1}{2}J^2R. \tag{2}$$

The first term represents convective or Peltier-like heat transport associated with charge flow, the second term is direct conductive heat leakage, and the third term is Joule dissipation.

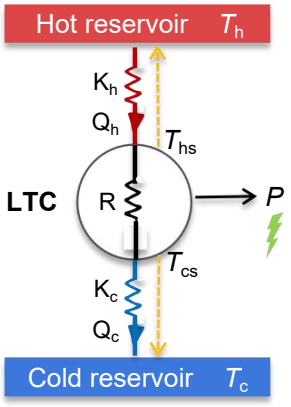


Figure 2. Schematic representation of the benchmark LTC model. K_h and K_c are the external thermal conductances at the hot and cold contacts, respectively, R is the intrinsic electrical resistance, and T_{hs}, T_{cs} are the local temperatures of the active region. Dashed arrows indicate the effective direction of Joule-heat release.

2.2. Asymmetric Joule-Heat Partition

To describe asymmetric heat release between the hot and cold sides, we introduce a spatially varying effective thermal conductivity:

$$\kappa(x) = \kappa_0\left(1 - \frac{x}{L}\right)^d, \tag{3}$$

where κ_0 is the conductivity at the hot side and d is a grading exponent. The profile in Equation (3) is not intended to be a literal conductivity distribution for all practical liquid-state thermocells. Instead, it is used as an analytically convenient representation that generates a tunable asymmetry in the terminal heat currents. The physically important quantity in the reduced model is the effective heat partition parameter ω, whereas the specific functional form of $\kappa(x)$ should be viewed as one possible mathematical route for obtaining asymmetric dissipation. Solving the one-dimensional heat equation with this profile (see Appendix A) leads to the generalized hot- and cold-side heat currents

$$\dot{Q}_h = JS_eT_{hs} + K(1-d)(T_{hs} - T_{cs}) - (1-\omega)J^2R, \tag{4}$$

$$\dot{Q}_c = JS_eT_{cs} + K(1-d)(T_{hs} - T_{cs}) + \omega J^2R, \tag{5}$$

where

$$\omega = \frac{1-d}{2-d}. \tag{6}$$

For the specific conductivity profile in Equation (3), the physically admissible range is restricted by the requirements that the effective conductive term remains non-negative and that ω can be interpreted as a heat partition fraction. These requirements lead to $d < 1$ for a finite positive effective conductance, with $d \to 1^-$ corresponding to the limiting case $\omega \to 0$. Values of $d > 1$ are not used in the physical interpretation of this profile because they would lead to a negative effective conductive term or to a heat fraction outside the interval $[0, 1]$. The parameter ω denotes the effective fraction of irreversible heat released to the cold side, while $1 - \omega$ corresponds to the fraction released to the hot side. Symmetric heat release corresponds to $\omega = 1/2$, whereas $\omega \neq 1/2$ describes directional asymmetry. In LTCs, ω should be regarded as an effective phenomenological parameter that summarizes the net directionality of irreversible heat release. It can represent, in a coarse-grained way, the combined influence of graded transport properties, asymmetric thermal coupling, electrode heat effects, non-uniform interfacial relaxation, and uneven spatial dissipation in the electrolyte−separator−electrode assembly. From a device design perspective, ω may be affected by experimentally tunable factors such as electrode material asymmetry, catalyst loading, electrode surface functionalization, separator thickness, electrolyte viscosity, redox concentration, and natural or forced convection.

Two limiting cases are of special interest. In the limiting case $d \to 1^-$, one has $\omega \to 0$, and the conductive leakage term tends to vanish. This limiting form corresponds to the ideal benchmark in which irreversible heat is effectively released to the hot side:

$$\dot{Q}_\mathrm{h} = JS_\mathrm{e}T_\mathrm{hs} - J^2R, \tag{7}$$

$$\dot{Q}_\mathrm{c} = JS_\mathrm{e}T_\mathrm{cs}. \tag{8}$$

The opposite limiting case, $\omega = 1$, cannot be obtained from the finite-d form of Equation (3). It is therefore introduced phenomenologically as an ideal benchmark representing the complete release of irreversible heat to the cold side. This limiting case is useful for establishing the lower performance bound and for comparing the thermodynamic consequences of hot-side and cold-side irreversible heat release:

$$\dot{Q}_\mathrm{h} = JS_\mathrm{e}T_\mathrm{hs}, \tag{9}$$

$$\dot{Q}_\mathrm{c} = JS_\mathrm{e}T_\mathrm{cs} + J^2R. \tag{10}$$

2.3. External Thermal Coupling and Performance Metrics

The LTC exchanges heat with the two reservoirs through finite thermal contacts. Assuming Newtonian heat transfer, we have

$$\dot{Q}_\mathrm{h} = K_\mathrm{h}(T_\mathrm{h} - T_\mathrm{hs}), \tag{11}$$

$$\dot{Q}_\mathrm{c} = K_\mathrm{c}(T_\mathrm{cs} - T_\mathrm{c}). \tag{12}$$

After imposing flux matching at both sides, the heat currents exchanged with the hot and cold reservoirs become

$$\dot{Q}_\mathrm{h} = K_\mathrm{h}\frac{JS_\mathrm{e}T_\mathrm{h} - (1-\omega)J^2R}{K_\mathrm{h} + JS_\mathrm{e}}, \tag{13}$$

$$\dot{Q}_c = K_c \frac{JS_eT_c + \omega J^2 R}{K_c - JS_e}. \tag{14}$$

The electrical power output is

$$P = \dot{Q}_h - \dot{Q}_c, \tag{15}$$

and the thermal efficiency is

$$\eta = \frac{P}{\dot{Q}_h}. \tag{16}$$

For convenience, we define

$$\delta = \frac{T_c}{T_h}, \qquad \eta_c = 1 - \delta, \tag{17}$$

and the ratio of external to internal thermal conductance, which is

$$\alpha = \frac{K_{ext}}{K_{int}}, \tag{18}$$

where

$$K_{ext} = \frac{K_h K_c}{K_h + K_c}, \tag{19}$$

$$K_{int} = \frac{S_e^2}{R}[\omega T_h + (1-\omega)T_c]. \tag{20}$$

The parameter α governs the relative importance of external thermal limitation and internal dissipation. A small α value corresponds to poor thermal contact and strong external irreversibility, while a large α value indicates nearly ideal thermal contacts and dominant internal irreversibility. The condition $\alpha = 1$ is referred to as thermal impedance matching, meaning that the effective external thermal conductance is comparable to the effective internal thermoelectrochemical conductance. Under this condition, neither the external thermal contact nor the internal dissipative transport dominates the overall finite-rate performance. It should be emphasized that K_{int} is not a purely conductive thermal conductance. Instead, it is an effective internal thermoelectrochemical conductance introduced within the lumped linear response description. It measures the strength of the coupling between electrical transport and heat transport through the redox-entropy-driven thermopower. The weighted temperature

$$T_\omega = \omega T_h + (1-\omega)T_c$$

represents the effective temperature level associated with the side receiving the dominant irreversible heat release. Thus, Equation (20) can be written as $K_{int} = S_e^2 T_\omega / R$. In contrast to solid-state thermoelectric generators, S_e in an LTC originates from thermoelectrochemical entropy changes, while R is a lumped resistance including ionic conduction, separator resistance, electrode contact resistance, and interfacial charge transfer resistance. Therefore, K_{int} should be interpreted as an effective parameterization for finite-rate thermodynamic analysis, rather than as a directly measured material conductance.

3. Results and Discussion

3.1. Exact Solutions for Four Representative Configurations

To retain analytical tractability while preserving clear physical meaning, we focused on four representative configurations. In each of them, only one thermal contact was finite

while the other was ideal, and the Joule heat was assumed to be fully released either to the hot side or to the cold side. These four cases served as benchmark LTC architectures.

3.1.1. Case I: Finite K_h with $\omega = 0$

In Case I, external irreversibility was located at the hot side, the cold-side contact was ideal ($K_c \to \infty$), and all Joule heat was released to the hot reservoir, as shown in Figure 3a. The heat currents reduced to

$$\dot{Q}_h = K_h \frac{JS_eT_h - J^2R}{K_h + JS_e}, \tag{21}$$

$$\dot{Q}_c = JS_eT_c. \tag{22}$$

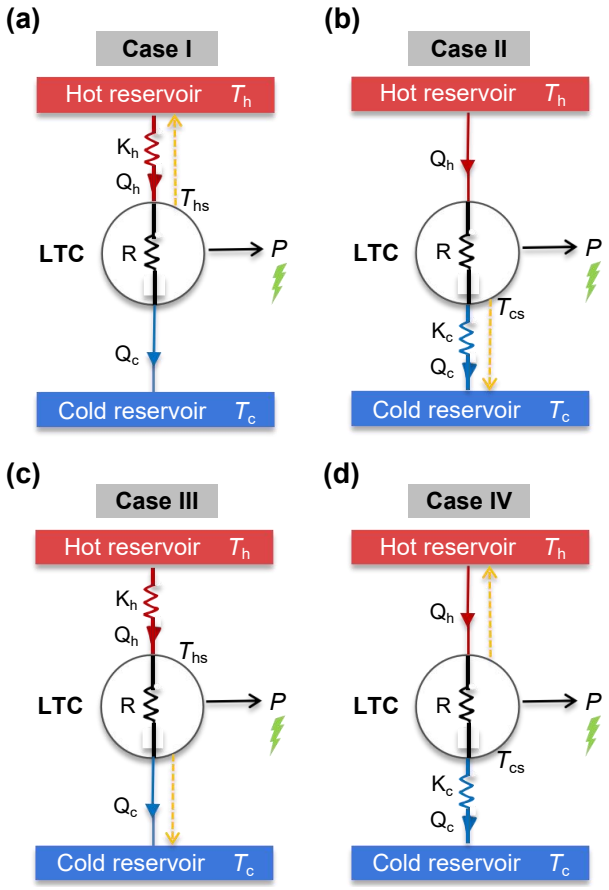


Figure 3. Four representative cases for LTC with coupled irreversibilities and dissipation. (**a**) Case I: finite hot-side heat conductance and Joule heat released to the hot side. (**b**) Case II: finite hot-side thermal conductance and Joule heat released to the cold side. (**c**) Case III: finite cold-side thermal conductance and Joule heat released to the cold side. (**d**) Case IV: finite cold-side thermal conductance and Joule heat released to the hot side.

Maximizing P with respect to J yields the EMP

$$\eta_I^* = \frac{\alpha + 1 - \sqrt{\delta(\alpha+1)(\alpha\delta+1)}}{\alpha + \alpha\delta + 1}, \tag{23}$$

with

$$\alpha = \frac{RK_h}{S_e^2T_c}, \tag{24}$$

and the corresponding maximum power

$$P_{\mathrm{I,max}} = K_{\mathrm{h}} T_{\mathrm{h}} \left[1 + 2\alpha\delta + \delta - 2\sqrt{\delta(\alpha+1)(\alpha\delta+1)} \right]. \tag{25}$$

The asymptotic limits are

$$\eta_{\mathrm{I}}^{*} \xrightarrow[\alpha\to 0]{} 1 - \sqrt{1-\eta_{\mathrm{c}}}, \qquad \eta_{\mathrm{I}}^{*} \xrightarrow[\alpha\to\infty]{} \frac{\eta_{\mathrm{c}}}{2-\eta_{\mathrm{c}}}, \tag{26}$$

such that

$$1 - \sqrt{1-\eta_{\mathrm{c}}} \le \eta_{\mathrm{I}}^{*} \le \frac{\eta_{\mathrm{c}}}{2-\eta_{\mathrm{c}}}. \tag{27}$$

This is the most favorable configuration for EMP within the present benchmark model, because both the external bottleneck and the Joule-heat feedback act on the hot side.

3.1.2. Case II: Finite K_{h} with $\omega = 1$

In Case II, the hot-side thermal contact is still finite, but all Joule heat is redirected to the cold side [see Figure 3b]:

$$\dot{Q}_{\mathrm{h}} = \frac{J S_{\mathrm{e}} K_{\mathrm{h}} T_{\mathrm{h}}}{K_{\mathrm{h}} + J S_{\mathrm{e}}}, \tag{28}$$

$$\dot{Q}_{\mathrm{c}} = J S_{\mathrm{e}} T_{\mathrm{c}} + J^2 R. \tag{29}$$

The efficiency at maximum power is

$$\eta_{\mathrm{II}}^{*} = 1 - \delta - (\alpha+\delta)A - \alpha A^2, \tag{30}$$

where

$$A = \frac{1}{6\alpha}\left[x^{1/3} + \frac{(2\alpha-\delta)^2}{x^{1/3}} - (4\alpha+\delta) \right], \tag{31}$$

$$x = 54\alpha^2 + (2\alpha-\delta)^3 + 6\sqrt{3}\,\alpha\sqrt{27\alpha^2 + (2\alpha-\delta)^3}, \tag{32}$$

and

$$\alpha = \frac{R K_{\mathrm{h}}}{S_{\mathrm{e}}^2 T_{\mathrm{h}}}. \tag{33}$$

The maximum power is

$$P_{\mathrm{II,max}} = K_{\mathrm{h}} T_{\mathrm{h}} \frac{A}{A+1}\left[1 - \delta - (\alpha+\delta)A - \alpha A^2 \right]. \tag{34}$$

Its limiting behavior is

$$\eta_{\mathrm{II}}^{*} \xrightarrow[\alpha\to 0]{} 1 - \sqrt{1-\eta_{\mathrm{c}}}, \qquad \eta_{\mathrm{II}}^{*} \xrightarrow[\alpha\to\infty]{} \frac{\eta_{\mathrm{c}}}{2}, \tag{35}$$

such that

$$\frac{\eta_{\mathrm{c}}}{2} \le \eta_{\mathrm{II}}^{*} \le 1 - \sqrt{1-\eta_{\mathrm{c}}}. \tag{36}$$

Compared with Case I, moving Joule heat from the hot side to the cold side significantly lowers the internal limit EMP.

3.1.3. Case III: Finite K_c with $\omega = 1$

In Case III, the hot-side contact is ideal, the cold-side contact is finite, and all Joule heat is released into the cold reservoir [see Figure 3c]:

$$\dot{Q}_h = JS_eT_h, \tag{37}$$

$$\dot{Q}_c = K_c\frac{JS_eT_c + J^2R}{K_c - JS_e}. \tag{38}$$

The resulting maximum power is

$$P_{III,max} = K_cT_h\left[1 + 2\alpha + \delta - 2\sqrt{(\alpha+1)(\alpha+\delta)}\right], \tag{39}$$

where

$$\alpha = \frac{RK_c}{S_e^2T_h}. \tag{40}$$

The corresponding EMP is

$$\eta^*_{III} = \alpha + 1 - \sqrt{(\alpha+1)(\alpha+\delta)}. \tag{41}$$

Its asymptotic behavior is

$$\eta^*_{III} \xrightarrow[\alpha\to 0]{} 1 - \sqrt{1-\eta_c}, \qquad \eta^*_{III} \xrightarrow[\alpha\to\infty]{} \frac{\eta_c}{2}, \tag{42}$$

and thus

$$\frac{\eta_c}{2} \le \eta^*_{III} \le 1 - \sqrt{1-\eta_c}. \tag{43}$$

This is the least favorable side placement from the viewpoint of EMP, because both the external bottleneck and the internal irreversible heat release act on the cold side.

3.1.4. Case IV: Finite K_c with $\omega = 0$

In Case IV, the cold-side thermal contact is finite, the hot-side contact is ideal, and all Joule heat is released to the hot side [see Figure 3d]:

$$\dot{Q}_h = JS_eT_h - J^2R, \tag{44}$$

$$\dot{Q}_c = \frac{JS_eK_cT_c}{K_c - JS_e}. \tag{45}$$

The efficiency at maximum power is

$$\eta^*_{IV} = 1 - \frac{\delta^2}{(\alpha B - 1)(B - \delta)}, \tag{46}$$

where

$$B = \frac{1}{6\alpha}\left[4\alpha\delta + 1 - y^{1/3} - \frac{(1-2\alpha\delta)^2}{y^{1/3}}\right], \tag{47}$$

$$y = 54\alpha^2\delta^3 + (2\alpha\delta - 1)^3 + 6\sqrt{3}\alpha\delta\sqrt{\delta[(2\alpha\delta-1)^3 + 27\alpha^2\delta^3]}, \tag{48}$$

and

$$\alpha = \frac{RK_c}{S_e^2T_c}. \tag{49}$$

The maximum power is

$$P_{\mathrm{IV,max}} = K_{\mathrm{c}} T_{\mathrm{h}} \frac{B(1-\alpha B)}{\delta}\left[1 - \frac{\delta^2}{(\alpha B - 1)(B-\delta)}\right]. \tag{50}$$

The limiting values are

$$\eta^*_{\mathrm{IV}} \xrightarrow[\alpha\to 0]{} 1 - \sqrt{1-\eta_{\mathrm{c}}}, \qquad \eta^*_{\mathrm{IV}} \xrightarrow[\alpha\to\infty]{} \frac{\eta_{\mathrm{c}}}{2-\eta_{\mathrm{c}}}, \tag{51}$$

and hence

$$1 - \sqrt{1-\eta_{\mathrm{c}}} \le \eta^*_{\mathrm{IV}} \le \frac{\eta_{\mathrm{c}}}{2-\eta_{\mathrm{c}}}. \tag{52}$$

Case IV provides an intermediate situation; the cold-side thermal resistance penalizes performance, but the release of Joule heat to the hot side preserves the higher internal limit EMP bound.

3.2. Operating Domain Constraints and Thermodynamic Consistency

For the benchmark model to remain physically meaningful, the operating current must stay within an admissible range. Since Equations (14), (38) and (45) contain the denominator $K_{\mathrm{c}} - JS_{\mathrm{e}}$, configurations with finite cold-side conductance require

$$0 < J < \frac{K_{\mathrm{c}}}{S_{\mathrm{e}}}. \tag{53}$$

In addition, for cases with $\omega = 0$, the positivity of the absorbed hot-side heat imposes

$$0 < J < \frac{S_{\mathrm{e}} T_{\mathrm{h}}}{R}. \tag{54}$$

Accordingly, a sufficient admissible domain is

$$0 < J < J_{\max}, \tag{55}$$

with

$$J_{\max} = \begin{cases} S_{\mathrm{e}} T_{\mathrm{h}}/R, & \text{Case I,} \\ +\infty, & \text{Case II,} \\ K_{\mathrm{c}}/S_{\mathrm{e}}, & \text{Case III,} \\ \min\left(K_{\mathrm{c}}/S_{\mathrm{e}},\ S_{\mathrm{e}} T_{\mathrm{h}}/R\right), & \text{Case IV.} \end{cases} \tag{56}$$

Within this domain, the optimized current J^* lies in the interior of the admissible interval for $\alpha > 0$ and $0 < \delta < 1$, and the stationary point corresponds to a genuine maximum of the power output. The second law is also respected. For example, in Case I, the entropy production rate can be written as follows:

$$\dot{\sigma} = -\frac{\dot{Q}_{\mathrm{h}}}{T_{\mathrm{h}}} + \frac{\dot{Q}_{\mathrm{c}}}{T_{\mathrm{c}}} = \frac{S_{\mathrm{e}}^2(\alpha\delta + 1)}{K_{\mathrm{h}} + JS_{\mathrm{e}}} J^2 > 0. \tag{57}$$

The corresponding entropy production expressions for Cases II–IV are provided in Appendix B. These expressions are positive within their admissible current domains, confirming the thermodynamic consistency of all four benchmark configurations.

3.3. Representative Parameter Ranges and Accessibility of Operating Regimes

To connect the reduced model with practical LTC systems, the representative orders of magnitude of the key parameters are summarized in Table 1. These values should not be interpreted as universal constants because they depend strongly on the electrode area, electrode spacing, electrolyte composition, separator structure, and thermal integration. Nevertheless, they indicate that the externally limited regime ($\alpha \ll 1$), the thermally matched regime ($\alpha \sim 1$), and the internally limited regime ($\alpha \gg 1$) can all be approached by changing either the external thermal contacts or the internal electrochemical resistance.

Table 1. Representative parameter ranges for liquid-state thermocells and their role in the present reduced model. The ranges are order-of-magnitude estimates for typical laboratory-scale aqueous thermocells and should be adjusted for specific cell geometries and electrolytes.

Parameter	Representative Range	Physical Meaning
S_e	10^{-4}–10^{-2} V K^{-1}	Thermoelectrochemical Seebeck coefficient
R	10^{-1}–10^{3} Ω	Lumped ionic and interfacial resistance
K	10^{-4}–10^{-1} W K^{-1}	Internal conductive heat leakage scale
K_h, K_c	10^{-4}–10^{0} W K^{-1}	External thermal-contact conductances
T_h	303–353 K	Hot reservoir temperature
T_c	283–323 K	Cold reservoir temperature
α	10^{-2}–10^{2}	External-to-internal thermal conductance ratio
ω	$0 < \omega < 1$	Effective fraction of irreversible heat released to cold side

3.4. Asymptotic Structure and EMP Hierarchy

Figure 4 compares the EMP of all four configurations for a representative Carnot efficiency $\eta_c = 0.5$. Although Figure 4 is plotted for $\eta_c = 0.5$, the analytical limiting expressions show that the same side-dependent trend is not specific to this representative value. The separation between the curves changed with the temperature ratio, but hot-side irreversible heat release remained less detrimental than cold-side release within the benchmark framework. A central result is that α controlled the transition between externally limited and internally limited operation. When $\alpha \to 0$, the effective external thermal conductance was much smaller than the internal one, and the system was dominated by thermal contact irreversibility. Therefore, all four cases converged to the Curzon–Ahlborn expression. By contrast, when $\alpha \to \infty$, the thermal contacts became effectively ideal, and internal dissipation dominated. In this limit, the asymptotic EMP depended on the side toward which irreversible heat was released. Cases I and IV, in which Joule heat was directed to the hot side, approached the upper bound $\eta_c/(2-\eta_c)$, whereas Cases II and III, in which Joule heat was directed to the cold side, approached the lower bound $\eta_c/2$.

This distinction is physically significant for LTC design. Releasing irreversible heat to the hot side is thermodynamically less detrimental than releasing it to the cold side, because the latter directly degrades the useful temperature gradient available for electrochemical power generation. At the same time, an external thermal resistance is less harmful when placed on the hot side than on the cold side. For finite operating values of α, the representative calculations indicate the following side-dependent hierarchy:

$$\eta_I^* > \eta_{IV}^* > \eta_{II}^* > \eta_{III}^*. \tag{58}$$

This inequality should be interpreted for finite operating regimes rather than for the limiting endpoints. As $\alpha \to 0$, all cases approached the Curzon–Ahlborn limit; as $\alpha \to \infty$, Cases I and IV shared the same upper asymptote, while Cases II and III shared the same

lower asymptote. Additional calculations for different values of η_c show that the qualitative hierarchy remained unchanged.

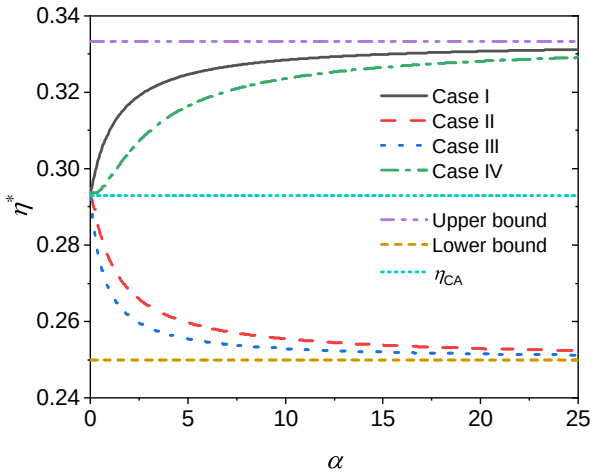


Figure 4. Efficiency at maximum power versus the external-to-internal thermal conductance ratio α for the four benchmark configurations, with $\eta_c = 0.5$. For $\alpha \to 0$, all cases recovered the Curzon−Ahlborn limit. For large α values, Cases I and IV approached the upper bound $\eta_c/(2-\eta_c)$, while Cases II and III approached the lower bound $\eta_c/2$.

3.5. Near-Equilibrium Behavior and Thermal Impedance Matching

Near thermal equilibrium ($\delta \to 1$), all four benchmark configurations satisfied the universal linear-response result

$$\eta^* = \frac{\eta_c}{2} + O(\eta_c^2), \tag{59}$$

independent of α. This universality is consistent with finite-time thermodynamics and confirms that the leading-order behavior of EMP does not depend on the detailed arrangement of irreversibilities under small temperature differences.

The distinctions among the four configurations appeared at the second order, especially under thermal impedance matching ($\alpha = 1$). The expansions are summarized in Table 2. For a fixed Joule-heat partition, moving the external thermal resistance from the hot side to the cold side lowered the second-order coefficient. Similarly, for a fixed side of external irreversibility, transferring Joule heat from the hot side to the cold side lowered the second-order EMP correction. These stepwise changes provide a compact way to quantify the side sensitivity of LTC performance.

Table 2. Efficiency at maximum power up to second order in η_c and optimal load ratio under thermal impedance matching ($\alpha = 1$).

Case	ω	$\eta^*(\alpha = 1)$	R^*_{load}/R at $\alpha = 1$
I	0	$\frac{\eta_c}{2} + \frac{6}{32}\eta_c^2 + O(\eta_c^3)$	2
II	1	$\frac{\eta_c}{2} + \frac{3}{32}\eta_c^2 + O(\eta_c^3)$	$2 + \frac{\eta_c}{2} + \frac{3}{32}\eta_c^2$
III	1	$\frac{\eta_c}{2} + \frac{2}{32}\eta_c^2 + O(\eta_c^3)$	2
IV	0	$\frac{\eta_c}{2} + \frac{5}{32}\eta_c^2 + O(\eta_c^3)$	$2 - \frac{\eta_c}{2} + \frac{19}{32}\eta_c^2$

3.6. Equivalent-Circuit Interpretation

For practical use, it is important to distinguish between the intrinsic resistance R of the LTC and the apparent internal resistance seen by the external load. The open-circuit electromotive force is

$$E_{oc} = S_e(T_{hs} - T_{cs}), \tag{60}$$

but T_{hs} and T_{cs} depend on the operating current because they are coupled to the thermal boundary conditions. Therefore, under load, the LTC cannot, in general, be represented by a simple current-independent Thevenin source with internal resistance exactly equal to R. Instead, the external circuit sees an apparent internal resistance that depends on the thermal coupling. If the external load is R_{load}, then

$$P = J^2 R_{load}. \tag{61}$$

For a generic Thevenin equivalent, maximum power is obtained when the load matches the apparent internal resistance and not necessarily the intrinsic resistance R. In the present benchmark model, this distinction becomes explicit. For Case I, substitution of the optimal current into the power relation gives

$$R^*_{load,I} = R\left(1 + \frac{1}{\alpha}\right). \tag{62}$$

Thus,

$$R^*_{load,I} \to R \qquad (\alpha \to \infty), \tag{63}$$

where the thermal contacts are nearly ideal, whereas

$$R^*_{load,I} \to \frac{S_e^2 T_c}{K_h} \qquad (\alpha \to 0), \tag{64}$$

where external thermal coupling governs the apparent matching condition. This resolves a common ambiguity in LTC equivalent-circuit discussions; the optimal electrical load generally depends on both electrical and thermal transport.

3.7. Implications for LTC Architecture

From the perspective of practical LTC design, the present results suggest several concrete strategies. First, when the device operates in the low-α regime, reducing external thermal contact resistance is more effective than solely lowering the internal electrical resistance. This can be achieved by improving heat exchanger contact, reducing encapsulation thermal resistance, and enhancing cold-side heat rejection. Second, the heat release pathway can be influenced by electrode asymmetry, catalyst loading, electrode surface functionalization, and separator design. These factors affect interfacial kinetics and local dissipation and therefore may shift the effective value of ω. Third, electrolyte engineering, including redox concentration, viscosity control, additives, and suppression or enhancement of convection, can modify both R and the spatial distribution of irreversible heat. Finally, the cold-side thermal management is particularly important because cold-side heat accumulation directly reduces the useful temperature span across the electrochemically active region.

3.8. Model Scope and Limitations

The present framework was intentionally reduced and benchmark-oriented. Several limitations should therefore be kept in mind. The Joule-heat partition parameter ω is phenomenological and does not explicitly resolve the microscopic origin of asymmetric heat

release. Concentration overpotentials, ion mass transfer limitations, electrolyte convection, side reactions, and long-term degradation were not included. In addition, only four exactly solvable one-contact finite configurations were treated analytically; the fully general case with finite K_h, finite K_c, and $0 < \omega < 1$ will generally require numerical optimization. Accordingly, the model should be interpreted as a thermodynamic benchmark rather than a full predictive simulator for a specific LTC chemistry.

The four configurations analyzed in this work should therefore be understood as limiting benchmark cases rather than as an exhaustive description of all possible LTC operating conditions. They were selected because they allowed closed-form expressions for maximum power, efficiency at maximum power, asymptotic limits, and load-matching conditions, thereby making the role of irreversibility placement transparent. A fully generalized treatment with simultaneous finite hot- and cold-side thermal contacts and intermediate heat partition $0 < \omega < 1$ would require numerical optimization over a larger parameter space, including K_h/K_c, ω, R, S_e, and the temperature ratio. Such an analysis is important but beyond the analytical scope of the present benchmark model. The spatial conductivity profile adopted in Appendix A is a mathematical device for deriving an analytically tractable heat partition relation. It should not be interpreted as a universal material prescription for practical LTC electrolytes or separators. In real devices, the same effective value of ω may result from electrode asymmetry, interfacial kinetics, electrolyte inhomogeneity, convection, or thermal contact asymmetry.

4. Conclusions

A finite-rate thermodynamic framework was developed for liquid-state thermocells operating under coupled internal and external irreversibilities. The model combines nonideal thermal contacts with an effective intrinsic electrical resistance and an asymmetric Joule-heat partition parameter, making it possible to analyze how the location of irreversibility affects the efficiency and power output of LTCs. Four benchmark configurations were solved analytically, yielding closed-form expressions for maximum power, efficiency at maximum power, asymptotic limits, and load-matching conditions. The analysis shows that the thermal impedance ratio α determines the transition between externally limited and internally limited operation. In the limit of dominant external irreversibility, all four cases recovered the Curzon–Ahlborn form. In the limit of dominant internal irreversibility, the asymptotic EMP depends on the side toward which irreversible heat is preferentially released; hot-side release led to the upper bound $\eta_c/(2-\eta_c)$, while cold-side release led to the lower bound $\eta_c/2$. Under thermal impedance matching, the second-order expansion of EMP revealed a clear hierarchy that further confirmed the thermodynamic advantage of locating both the dominant external bottleneck and the dominant irreversible heat release at the hot side. These findings provide a useful benchmark for the LTC architecture and thermal management. They indicate that sink-side thermal crowding and cold-side irreversible heating should be avoided, while electrical load matching must be interpreted together with the thermal environment. More broadly, the present framework clarifies how coupled irreversibilities shape the trade-off between power and efficiency in liquid-state electrochemical heat engines. Future work should extend the model by incorporating concentration polarization, coupled mass and heat transfer, interfacial reaction kinetics, and multiphysics validation against experimental LTC systems. In addition, the fully generalized finite-contact case with finite K_h, finite K_c, and intermediate heat partition $0 < \omega < 1$ should be examined through numerical optimization to test the robustness of the analytical hierarchy beyond the four limiting configurations. Such developments would help bridge the gap between analytical thermodynamic bounds and device-specific design.

https://doi.org/10.3390/thermo6020041

Author Contributions: Conceptualization, X.W.; methodology, X.W.; software, X.W.; validation, Z.Y.; formal analysis, X.W., Z.Y. and Y.Y.; investigation, X.W., Z.Y. and Y.Y.; resources, X.W.; data curation, Y.Y.; writing—original draft preparation, X.W.; writing—review and editing, Z.Y. and Y.Y.; visualization, X.W.; supervision, X.W.; project administration, X.W.; funding acquisition, X.W. All authors have read and agreed to the published version of the manuscript.

Funding: This research was funded by the Startup Foundation for doctors of Yan'an University under Grant YDBK2022-72 and the Key Scientific Research Plan Project of the Education Department of Shaanxi Province under Grant 25JS137 .

Data Availability Statement: All data, models, and code that support the findings of this study are available from the corresponding author upon reasonable request.

Conflicts of Interest: The authors declare no conflicts of interest.

Abbreviations

The following abbreviations are used in this manuscript:

LTC	Liquid-state thermocell
EMP	Efficiency at maximum power

Appendix A. Derivation of the Internal Heat Currents with Spatially Varying Conductivity

For completeness, the derivation of Equations (4) and (5) is briefly summarized here. The local heat flux in the active LTC region is written as follows:

$$\boldsymbol{j}_Q = S_e \boldsymbol{j} T - \kappa(x) \nabla T, \tag{A1}$$

where $\boldsymbol{j}$ is the electric flux and $\kappa(x)$ is the effective local thermal conductivity. The local balance of energy gives

$$\nabla \cdot \boldsymbol{j}_Q = \boldsymbol{j} \cdot \boldsymbol{E}, \tag{A2}$$

while the Onsager constitutive relation is

$$\boldsymbol{j} = \sigma_{\text{eff}} \boldsymbol{E} - S_e \sigma_{\text{eff}} \nabla T, \tag{A3}$$

with σ_{eff} being the effective electrical conductivity. In one dimension, combining Equations (A1)–(A3) yields

$$\kappa(x) \frac{d^2T}{dx^2} + \frac{d\kappa(x)}{dx} \frac{dT}{dx} = -\frac{j^2}{\sigma_{\text{eff}}}, \tag{A4}$$

where j is the magnitude of the current density.

Assuming that

$$\kappa(x) = \kappa_0 \left(1 - \frac{x}{L}\right)^d, \tag{A5}$$

with boundary conditions $T(0) = T_{\text{hs}}$ and $T(L) = T_{\text{cs}}$, integration gives

$$\frac{dT}{dx} = -\frac{j^2 x}{\sigma_{\text{eff}} \kappa_0 (1 - x/L)^d} - \frac{(1-d)(T_{\text{hs}} - T_{\text{cs}})}{L(1 - x/L)^d} + \frac{j^2 L}{\sigma_{\text{eff}} \kappa_0 (2-d)(1 - x/L)^d}. \tag{A6}$$

The grading exponent d cannot be chosen arbitrarily. For the profile in Equation (A5), a finite and positive effective conductance requires $d < 1$. The limiting case $d \to 1^-$ gives $\omega \to 0$ and suppresses the conductive leakage term. Therefore, the relation $\omega = (1-d)/(2-d)$ is used here only within its physically admissible domain, rather than as a universal expression for all possible heat partition states.

For a spatially varying thermal conductivity, the effective conductive thermal conductance is

$$K_{\mathrm{eff}} = \frac{A}{\int_0^L \frac{dx}{\kappa(x)}}. \tag{A7}$$

Substituting Equation (A5) into Equation (A7) gives

$$K_{\mathrm{eff}} = \frac{\kappa_0 A}{L}(1-d) = K(1-d), \qquad d < 1. \tag{A8}$$

This result explains the appearance of the factor $K(1-d)$ in the terminal heat current expressions. When introducing $J = jA$, $R = L/(\sigma_{\mathrm{eff}}A)$, and $K = \kappa_0 A/L$, the endpoint heat fluxes are

$$\dot{Q}_{\mathrm{h}} = JS_{\mathrm{e}}T_{\mathrm{hs}} + K(1-d)(T_{\mathrm{hs}} - T_{\mathrm{cs}}) - (1-\omega)J^2R, \tag{A9}$$

$$\dot{Q}_{\mathrm{c}} = JS_{\mathrm{e}}T_{\mathrm{cs}} + K(1-d)(T_{\mathrm{hs}} - T_{\mathrm{cs}}) + \omega J^2R, \tag{A10}$$

where

$$\omega = \frac{1-d}{2-d}. \tag{A11}$$

In the limiting case $d \to 1^-$, the conductive leakage term tends to vanish and $\omega \to 0$, leading to the simplified hot-side release benchmark used in Cases I and IV.

Appendix B. Entropy Production Expressions for the Four Benchmark Cases

The entropy production rate is defined as follows:

$$\dot{\sigma} = -\frac{\dot{Q}_{\mathrm{h}}}{T_{\mathrm{h}}} + \frac{\dot{Q}_{\mathrm{c}}}{T_{\mathrm{c}}}. \tag{A12}$$

For Case I, substituting Equations (21) and (22) into Equation (A12) gives

$$\dot{\sigma}_{\mathrm{I}} = \frac{J^2}{K_{\mathrm{h}} + JS_{\mathrm{e}}}\left(S_{\mathrm{e}}^2 + \frac{K_{\mathrm{h}}R}{T_{\mathrm{h}}}\right) > 0. \tag{A13}$$

For Case II, one obtains

$$\dot{\sigma}_{\mathrm{II}} = J^2\left[\frac{S_{\mathrm{e}}^2}{K_{\mathrm{h}} + JS_{\mathrm{e}}} + \frac{R}{T_{\mathrm{c}}}\right] > 0. \tag{A14}$$

For Case III, the entropy production rate is

$$\dot{\sigma}_{\mathrm{III}} = \frac{J^2}{K_{\mathrm{c}} - JS_{\mathrm{e}}}\left(S_{\mathrm{e}}^2 + \frac{K_{\mathrm{c}}R}{T_{\mathrm{c}}}\right) > 0, \qquad 0 < J < \frac{K_{\mathrm{c}}}{S_{\mathrm{e}}}. \tag{A15}$$

For Case IV, one obtains

$$\dot{\sigma}_{\mathrm{IV}} = J^2\left[\frac{R}{T_{\mathrm{h}}} + \frac{S_{\mathrm{e}}^2}{K_{\mathrm{c}} - JS_{\mathrm{e}}}\right] > 0, \qquad 0 < J < \frac{K_{\mathrm{c}}}{S_{\mathrm{e}}}. \tag{A16}$$

Equations (A13)–(A16) show that all four benchmark configurations satisfy the second law within their corresponding admissible current domains.

References

1. Xiao, D.; Xiao, H.; Song, W.; Li, G.; Zhang, J.; Deng, H.; Guo, B.; Tang, G.; Duan, M.; Tang, H. Utilization method of low-grade thermal energy during drilling based on insulated Drill pipe. *Renew. Energy* **2024**, *225*, 120363. [CrossRef]
2. Kumar, R.; Lee, D.; Ağbulut, Ü.; Kumar, S.; Thapa, S.; Thakur, A.; Jilte, R.; Saleel, C.A.; Shaik, S. Different energy storage techniques: Recent advancements, applications, limitations, and efficient utilization of sustainable energy: R. Kumar et al. *J. Therm. Anal. Calorim.* **2024**, *149*, 1895–1933. [CrossRef]
3. Ji, D.; Liu, G.; Romagnoli, A.; Rajoo, S.; Besagni, G.; Markides, C.N. Low-grade thermal energy utilization: Technologies and applications. *Appl. Therm. Eng.* **2024**, *244*, 122618. [CrossRef]
4. Liu, G.; Ji, D.; Markides, C.N. Progress and prospects of low-grade thermal energy utilization technologies. *Appl. Therm. Eng.* **2024**, *254*, 123859. [CrossRef]
5. Sheikholeslami, M.; Khalili, Z. Investigation of nanofluid cooling influence on energy performance of photovoltaic-thermoelectric module. *J. Therm. Anal. Calorim.* **2024**, *149*, 495–503. [CrossRef]
6. Li, Z.; Qian, G.; Shen, Z.; Shen, Y.; Huang, Y.; Jiang, R.; Huang, R.; Yu, X. Effects of operating parameters for low-grade heat driven thermo-electrochemical cells based on orthogonal experiments. *Appl. Therm. Eng.* **2024**, *243*, 122664. [CrossRef]
7. XiaHou, X.; Zhang, X.; Rahman, E.; Chen, X. Performance enhancement of a high-temperature proton exchange membrane fuel cell through energy recovery of a near-field thermoradiative cell. *Energy Convers. Manag.* **2026**, *348*, 120681. [CrossRef]
8. Chen, H.; Zou, H.; Zhong, F.; Qu, M.; Zhao, S.; Wei, X.; Hong, D.; Song, Y.; Liu, Z. Liquid-flow thermocells with high hybrid entropy for low-grade heat harvesting. *Nano Energy* **2024**, *129*, 109992. [CrossRef]
9. Xiang, Y.; Guo, X.; Zhu, H.; Zhang, Q.; Zhu, S. Aqueous biphase-boosted liquid-state thermocell for continuous low-grade heat harvesting. *Chem. Eng. J.* **2023**, *461*, 142018. [CrossRef]
10. Wang, M.; Ruan, J.; Tao, F.; Zhu, J.; Zhang, Y.; Xiong, Y.; Zhang, X.; Ang, Y.S. A technically feasible strategy using liquid-state thermocells to efficiently recover the waste heat released from proton exchange membrane fuel cells. *Energy Convers. Manag.* **2023**, *294*, 117541. [CrossRef]
11. Zhou, H.; Matsuno, R.; Wakayama, Y.; Du, J.; Yamada, T. Application of bipolar electrodes in thermocells for efficient waste-heat recovery. *J. Power Sources* **2024**, *614*, 235048. [CrossRef]
12. Liu, X.; Wang, T.; Fang, J.; Fan, F.R. Self-reaction effect-boosted liquid thermocell based on ethanol-aqueous biphasic system. *Adv. Mater. Technol.* **2023**, *8*, 2300988. [CrossRef]
13. Zhu, H.; Chen, S.; Zhang, H. Performance prediction and manipulation strategy of a hybrid system based on tubular solid oxide fuel cell and annular thermoelectric generator. *J. Non-Equilib. Thermodyn.* **2025**, *50*, 149–172. [CrossRef]
14. Yu, X.; Shen, Z.; Qian, G.; Lu, G.; Liu, H.; Huang, R.; Li, Z. Synergistic improvement of Seebeck coefficient and power density of an aqueous thermocell using natural convection for low-grade heat utilization. *Appl. Therm. Eng.* **2023**, *231*, 121004. [CrossRef]
15. Ye, F.; Zhao, X.; Zhang, Y.; Man, Y.; Qi, F.; Zhang, X.; Peng, W.; Rahman, E.; Guo, J. Efficiency enhancement of photovoltaic modules via full-spectrum utilization and waste heat recovery using liquid-state thermocells. *Renew. Energy* **2025**, *256*, 124247. [CrossRef]
16. Wang, M.; Ruan, J.; Zhang, J.; Jiang, Y.; Gao, F.; Zhang, X.; Rahman, E.; Guo, J. Modeling, thermodynamic performance analysis, and parameter optimization of a hybrid power generation system coupling thermogalvanic cells with alkaline fuel cells. *Energy* **2024**, *292*, 130557. [CrossRef]
17. Shen, Y.; Qian, G.; Yu, X.; Li, Z.; Huang, Y. Numerical study on heat and ion transport characteristics enables optimal design of aqueous thermocells for low-grade heat recovery. *Appl. Therm. Eng.* **2025**, *260*, 124970. [CrossRef]
18. Yu, B.; Duan, J.; Cong, H.; Xie, W.; Liu, R.; Zhuang, X.; Wang, H.; Qi, B.; Xu, M.; Wang, Z.L.; et al. Thermosensitive crystallization–boosted liquid thermocells for low-grade heat harvesting. *Science* **2020**, *370*, 342–346. [CrossRef]
19. Mao, Q.; Wang, Y.; Li, H.; Zhang, X.; Rahman, E. Toward full-spectrum solar energy utilization via synergistic coupling of perovskite solar cells and liquid-state thermocells. *Renew. Energy* **2026**, *270*, 125893. [CrossRef]
20. Gao, F.; Zhang, X.; Rahman, E.; Guo, J. Performance evaluation and optimal design of solar thermal liquid thermogalvanic generators without optical concentrator. *Sol. Energy* **2026**, *303*, 114122. [CrossRef]
21. He, X.; Sun, H.; Li, Z.; Chen, X.; Wang, Z.; Niu, Y.; Jiang, J.; Wang, C. Redox-induced thermocells for low-grade heat harvesting: Mechanism, progress, and their applications. *J. Mater. Chem.* **2022**, *10*, 20730–20755. [CrossRef]
22. Chen, L.; Xia, S. Maximum work configuration of finite potential source endoreversible non-isothermal chemical engines. *J. Non-Equilib. Thermodyn.* **2023**, *48*, 41–53. [CrossRef]
23. Duan, J.; Yu, B.; Huang, L.; Hu, B.; Xu, M.; Feng, G.; Zhou, J. Liquid-state thermocells: Opportunities and challenges for low-grade heat harvesting. *Joule* **2021**, *5*, 768–779. [CrossRef]
24. Hu, C.; Chen, L.; Ge, Y.; Feng, H. Single-, two-, three-, and four-objective optimizations for an irreversible vacuum thermionic generator via finite-time thermodynamics, NSGA-II and three decision-making techniques. *J. Non-Equilib. Thermodyn.* **2025**, *50*, 615–628. [CrossRef]

25. Wu, B.; Chen, L.; Ge, Y.; Feng, H.; Liu, X. Finite-time thermodynamic multi-objective optimizations for an irreversible simple Brayton refrigeration cycle based on four objectives, NASG-II algorithm and three decision-making strategies. *J. Therm. Anal. Calorim.* **2025**, *150*, 4653–4668. [CrossRef]
26. Chen, L.; Xia, S.; Shi, S. Maximizing work of finite-potential-reservoir isothermal-chemical-engines with generalized models of bypass-mass-leakage and mass-resistance. *J. Therm. Anal. Calorim.* **2024**, *149*, 11817–11825. [CrossRef]
27. Curzon, F.L.; Ahlborn, B. Efficiency of a Carnot engine at maximum power output. *Am. J. Phys.* **1975**, *43*, 22–24. [CrossRef]
28. Schmiedl, T.; Seifert, U. Efficiency of molecular motors at maximum power. *Europhys. Lett.* **2008**, *83*, 30005. [CrossRef]
29. Schmiedl, T.; Seifert, U. Efficiency at maximum power: An analytically solvable model for stochastic heat engines. *Europhys. Lett.* **2007**, *81*, 20003. [CrossRef]
30. Chen, L.; Qi, C.; Ge, Y.; Feng, H. Thermal Brownian heat engine with external and internal irreversibilities. *Energy* **2022**, *255*, 124582. [CrossRef]
31. Apertet, Y.; Ouerdane, H.; Goupil, C.; Lecoeur, P. Irreversibilities and efficiency at maximum power of heat engines: The illustrative case of a thermoelectric generator. *Phys. Rev. E—Stat. Nonlinear Soft Matter Phys.* **2012**, *85*, 031116. [CrossRef]
32. Qi, C.; Chen, L.; Feng, H.; Ge, Y.; Chen, X. Modeling and performance evaluation for solar thermoelectric generator with variable-temperature heat sink. *Appl. Therm. Eng.* **2025**, *274*, 126770. [CrossRef]
33. Meng, F.; Chen, L.; Sun, F. A numerical model and comparative investigation of a thermoelectric generator with multi-irreversibilities. *Energy* **2011**, *36*, 3513–3522. [CrossRef]
34. Kaur, J.; Johal, R.S. Thermoelectric generator at optimal power with external and internal irreversibilities. *J. Appl. Phys.* **2019**, *126*, 125111. [CrossRef]
35. He, D.; Tang, X.; Rehan, M.A.; Li, G. Heat and mass transfer performance of ferricyanide/ferrocyanide thermocell and optimization analysis. *Energy* **2024**, *289*, 129973. [CrossRef]
36. Holtan, H., Jr.; Mazur, P.; De Groot, S. On the theory of thermocouples and thermocells. *Physica* **1953**, *19*, 1109–1118. [CrossRef]
37. Ratkje, S.K.; Ikeshoji, T.; Syverud, K. Heat and internal energy changes at electrodes and junctions in thermocells. *J. Electrochem. Soc.* **1990**, *137*, 2088–2095. [CrossRef]
38. Onsager, L. Reciprocal relations in irreversible processes. I. *Phys. Rev.* **1931**, *37*, 405. [CrossRef]
39. Callen, H.B. The application of Onsager's reciprocal relations to thermoelectric, thermomagnetic, and galvanomagnetic effects. *Phys. Rev.* **1948**, *73*, 1349. [CrossRef]
40. Domenicali, C.A. Irreversible thermodynamics of thermoelectricity. *Rev. Mod. Phys.* **1954**, *26*, 237. [CrossRef]
41. Apertet, Y.; Ouerdane, H.; Goupil, C.; Lecoeur, P. From local force-flux relationships to internal dissipations and their impact on heat engine performance: The illustrative case of a thermoelectric generator. *Phys. Rev. E—Stat. Nonlinear Soft Matter Phys.* **2013**, *88*, 022137. [CrossRef]

Disclaimer/Publisher's Note: The statements, opinions and data contained in all publications are solely those of the individual author(s) and contributor(s) and not of MDPI and/or the editor(s). MDPI and/or the editor(s) disclaim responsibility for any injury to people or property resulting from any ideas, methods, instructions or products referred to in the content.